



Publication Year	2022
Acceptance in OA	2022-06-16T10:23:01Z
Title	The Smallest Scale of Hierarchy Survey (SSH). II. Extended star formation and bar-like features in the dwarf galaxy NGC 3741: recent merger or ongoing gas accretion?
Authors	ANNIBALI, FRANCESCA, BACCHINI, CECILIA, Iorio, Giuliano, BELLAZZINI, Michele, PASCALE, Raffaele, BECCARI, GIACOMO, Cignoni, Michele, Ciotti, NIPOTI, CARLO, Sacchi, Elena, TOSI, Monica, CUSANO, FELICE, Bisogni, Susanna, GARGIULO, ADRIANA, PARIS, Diego
Publisher's version (DOI)	10.1093/mnras/stac541
Handle	http://hdl.handle.net/20.500.12386/32348
Journal	MONTHLY NOTICES OF THE ROYAL ASTRONOMICAL SOCIETY
Volume	512

The Smallest Scale of Hierarchy Survey (SSH) – II. Extended star formation and bar-like features in the dwarf galaxy NGC 3741: recent merger or ongoing gas accretion?

F. Annibali ¹★, C. Bacchini ²★, G. Iorio ^{2,3,4}, M. Bellazzini ¹, R. Pascale ^{1,5}, G. Beccari ⁶,
M. Cignoni ⁷, L. Ciotti ⁵, C. Nipoti ⁵, E. Sacchi ^{1,8}, M. Tosi ¹, F. Cusano ¹, S. Bisogni ⁹, A. Gargiulo ⁹
and D. Paris ¹⁰

¹INAF - Osservatorio di Astrofisica e Scienza dello Spazio, Via Piero Gobetti, 93/3, I-40129 Bologna, Italy

²INAF - Osservatorio Astronomico di Padova, vicolo dell'Osservatorio 5, I-35122 Padova, Italy

³Dipartimento di Fisica e Astronomia 'Galileo Galilei', Università di Padova, vicolo dell'Osservatorio 3, I-35122 Padova, Italy

⁴INFN-Padova, Via Marzolo 8, I-35131 Padova, Italy

⁵Dipartimento di Fisica e Astronomia, Università di Bologna, via Piero Gobetti 93/2, I-40129 Bologna, Italy

⁶ESO, Karl-Schwarzschild Strasse 2, D-80 Garching, Germany

⁷Dipartimento di Fisica, Università di Pisa, Largo Bruno Pontecorvo 3, I-56127 Pisa, Italy

⁸Leibniz-Institut für Astrophysik Potsdam, An der Sternwarte 16, I-14482 Potsdam, Germany

⁹INAF Istituto di Astrofisica Spaziale e Fisica Cosmica di Milano, Via Alfonso Corti 12, I-20133 Milano, Italy

¹⁰INAF - Osservatorio Astronomico di Roma, via Frascati 33, I-00078 Monte Porzio Catone (RM), Italy

Accepted 2022 February 23. Received 2022 February 23; in original form 2021 November 22

ABSTRACT

Using Large Binocular Telescope deep imaging data from the Smallest Scale of Hierarchy Survey (SSH) and archival *Hubble Space Telescope* data, we reveal the presence of two elongated stellar features contiguous to a bar-like stellar structure in the inner regions of the dwarf irregular galaxy NGC 3741. These structures are dominated by stars younger than a few hundred Myr and collectively are about twice as extended as the old stellar component. These properties are very unusual for dwarf galaxies in the nearby Universe and difficult to explain by hydro-dynamical simulations. From the analysis of archival 21-cm observations, we find that the young stellar ‘bar’ coincides with an HI high-density region proposed by previous studies to be a purely gaseous bar; we furthermore confirm radial motions of a few km s⁻¹, compatible with an inflow/outflow, and derive a steeply rising rotation curve and high HI surface density at the centre, indicating a very concentrated mass distribution. We propose that the peculiar properties of the stellar and gaseous components of NGC 3741 may be explained by a recent merger or ongoing gas accretion from the intergalactic medium, which caused gas inflows towards the galaxy centre and triggered star formation a few hundred Myr ago. This event may explain the young and extended stellar features, the bar-like structure, the very extended HI disc and the central HI spiral arms. The high central HI density and the steeply rising rotation curve suggest that NGC 3741 may be the progenitor or the descendant of a starburst dwarf.

Key words: galaxies: dwarf – galaxies: formation – galaxies: individuals: NGC 3741 – galaxies: interactions – galaxies: irregular – galaxies: stellar content.

1 INTRODUCTION

In the Λ cold dark matter (Λ CDM) cosmological scenario (Peebles et al. 1982), galaxies are assembled over time through the accretion of smaller systems (White 1978). Observational evidence of this hierarchical formation process is the presence of numerous satellites and stellar streams around massive galaxies in the Local Volume (e.g. Belokurov et al. 2006; McConnachie et al. 2009; Martínez-Delgado et al. 2010; Crnojević et al. 2016; Ibata et al. 2021; Malhan et al. 2021). Numerical simulations predict that the merger activity continues down to the lower mass scales of dwarf galaxies (Diemand

et al. 2008; Deason, Wetzel & Garrison-Kimmel 2014; Wheeler et al. 2015); nevertheless, dwarf–dwarf galaxy mergers have received little attention from the observational point of view so far, mostly because of the difficulty in detecting very low surface brightness merger signatures around these systems. Merger or interaction events can strongly impact the evolution of dwarf galaxies, affecting their morphology and kinematics, and providing a viable mechanism to trigger gas flows towards the inner galaxy regions and, possibly, the onset of a starburst (Bekki 2008; Stierwalt et al. 2015; Carlin et al. 2016; Privon et al. 2017; Kado-Fong et al. 2020). A number of individual dwarf–dwarf merger cases has been examined in the literature (Rich et al. 2012; Martínez-Delgado et al. 2012; Amorisco, Evans & van de Ven 2014; Sand et al. 2015; Belokurov & Koposov 2016; Annibali et al. 2016; Privon et al. 2017; Kallivayalil et al.

* E-mail: francesca.annibali@inaf.it (FA); cecilia.bacchini@inaf.it (CB)

Table 1. Properties of NGC 3741.

Property	Value	References
Distance	3.2 Mpc	1
Stellar mass	$3.8 \times 10^7 M_{\odot}$	2
Exponential disc scale length	0.20 kpc	3
H I mass	$1.3 \times 10^8 M_{\odot}$	4
Rotation velocity	50 km s^{-1}	3, 4
Inclination	$68 \pm 4^{\circ}$	4, 5
SFR	$(4.3 \pm 0.7) \times 10^{-3} M_{\odot} \text{ yr}^{-1}$	6, 7
SFR surface density	$3.2 \times 10^{-4} M_{\odot} \text{ yr}^{-1} \text{ kpc}^{-2}$	8
$12 + \log(O/H)$	7.68 ± 0.03	9

The last column reports the reference papers: 1 = Tully et al. (2006); 2 = Weisz et al. (2011); 3 = Lelli et al. (2016); 4 = Gentile et al. (2007); 5 = Begum et al. (2005); 6 = Karachentsev & Kaisina (2013); 7 = Begum et al. (2008); 8 = Roychowdhury, Chengalur & Shi (2017); 9 = Berg et al. (2012).

2018; Makarova et al. 2018; Johnston et al. 2019; Zhang et al. 2020), but only a few systematic searches for dwarfs companions have been conducted so far (Stierwalt et al. 2015; Carlin et al. 2016; Higgs et al. 2016; Paudel et al. 2018; Annibali et al. 2020; Kado-Fong et al. 2020)

The Smallest Scale of Hierarchy Survey (SSH; Annibali et al. 2020) is an observational campaign designed to characterize the frequency and properties of interaction and merging events around a large sample of dwarf galaxies. SSH exploits the high sensitivity and very large field of view ($\approx 23 \times 23 \text{ arcmin}^2$) of the Large Binocular Channel (LBC) on the Large Binocular Telescope (LBT). It provides deep *g* and *r* photometry for 45 late-type dwarfs at distances between ~ 1 and ~ 10 Mpc down to a surface brightness limit of $\mu_r \sim 31 \text{ mag arcsec}^{-2}$. The SSH targets span a wide range in luminosity, from about twice the luminosity of the Large Magellanic Cloud (LMC) down to about 5 mag fainter, and cover a wide range of density environments, from very isolated galaxies to group members. Photometry in two bands allows us to define the colour–magnitude diagrams (CMDs) and to separate, for targets closer than $\sim 4\text{--}5$ Mpc, red giant branch (RGB) stars associated with the dwarf galaxy or with a potential satellite from background contaminants. This technique permits to reveal faint stellar substructures (e.g. streams and shells) or companions around the dwarfs. The LBC field of view translates into an explored physical region of $\sim 7 \times 7$ to $\sim 70 \times 70 \text{ kpc}^2$, depending on the galaxy distance.

In this paper, we present new results for the galaxy NGC 3741 (see Table 1 for a summary of the main properties), which was observed as part of the SSH survey. NGC 3741 is a dwarf irregular (dIrr) galaxy located at a distance of ~ 3.2 Mpc (Tully et al. 2006; Dalcanton et al. 2009, i.e. $1 \text{ arcsec} = 15.7 \text{ pc}$) and has an absolute blue magnitude of $M_B = -13.2$ (Cook et al. 2014). NGC 3741 belongs to the Canes Venatici I galaxy cloud, which is located at the periphery of the M 81 group. NGC 3741 is supposed to be quite undisturbed by other galaxies (Karachentsev et al. 2003, 2004), being at a de-projected distance of $\simeq 1.65$ Mpc from M 81 (Karachentsev et al. 2002).

One of the most remarkable properties of NGC 3741 is the extent of the H I disc. Indeed, 21-cm observations with the Giant Meterwave Radio Telescope (GMRT) by Begum, Chengalur & Karachentsev (2005) and with the Westerbork Synthesis Radio Telescope (WSRT) by Gentile et al. (2007) revealed that the diameter of the H I disc is $\gtrsim 14 \text{ arcmin}$ ($\sim 13 \text{ kpc}$) at H I column density $N_{\text{HI}} \sim 10^{19} \text{ cm}^{-2}$ ($\sim 0.1 M_{\odot} \text{ pc}^{-2}$). The H I disc diameter is ~ 21 times larger than the *B*-band half-light diameter, which is $\sim 40 \text{ arcsec}$ or $\sim 0.6 \text{ kpc}$ (de

Vaucouleurs et al. 1991). The total H I mass is $M_{\text{HI}} \sim 1.3 \times 10^8 M_{\odot}$ (Gentile et al. 2007; Begum et al. 2008), which is about 3.4 times larger than the stellar mass ($M_{\star} \sim 3.8 \times 10^7$; Weisz et al. 2011).

The decomposition of the rotation curve of NGC 3741 into the contribution of the individual mass components (i.e. stellar disc, gas disc, and dark matter halo) indicates that the galaxy gravitational potential is dominated by dark matter (Begum et al. 2005; Gentile et al. 2007; Allaert, Gentile & Baes 2017). The baryonic and dark matter mass estimates for NGC 3741 are consistent with scaling relations derived for dwarf galaxies (e.g. Lelli, McGaugh & Schombert 2016; McGaugh, Lelli & Schombert 2016; Thuan et al. 2016; Iorio et al. 2017; Posti et al. 2018; Mancera Piña et al. 2019; Romeo 2020; Romeo, Agertz & Renaud 2020). Gentile et al. (2007) analysed the kinematics of the H I disc and argued that the innermost part of the rotation curve is better reproduced by a cored dark matter profile (in which case baryons dominate the inner gravitational potential) rather than by a cuspy one. Nevertheless, the high uncertainty in the inner rotation curve, due to the presence of non-circular motion, implies that a cuspy dark matter halo cannot be definitively ruled out (e.g. Hayashi & Navarro 2006; Gentile et al. 2007; Randriamampandry et al. 2015; Oman et al. 2019).

Moreover, Gentile et al. (2007) found that, despite the overall symmetry of the velocity field, this is distorted by non-circular motions of the order of $5\text{--}13 \text{ km s}^{-1}$. These motions were ascribed to the presence of a H I bar in the inner regions (see also Begum et al. 2005; Banerjee et al. 2013) and ongoing accretion of gas in the outer parts of the galaxy. Another interesting feature of the H I disc of NGC 3741 is the presence of spiral arms originating from the bar region (Gentile et al. 2007; Begum et al. 2008; Ott et al. 2012). Interestingly, while the spiral arms and the bar are visible from the atomic gas distribution, no stellar counterpart is observed (e.g. Vaduvescu et al. 2005), suggesting that NGC 3741 is one of the few galaxies with purely gaseous bar and spiral arms. Bars may either form spontaneously as a consequence of disc instability (e.g. see Athanassoula 2013, for a review) or in response to an interaction with a galaxy companion (Gajda, Łokas & Athanassoula 2018; Pettitt & Wadsley 2018). They can also be boosted and renewed by cold gas accretion (Combes 2014). However, the formation of purely gaseous bars remains a mystery. For instance, Gajda et al. (2018) used numerical simulations to investigate the formation of tidally induced bars in gas-rich dwarf galaxies and found that, while bars are formed in the stellar component, no trace of the bar is found in the gaseous component.

Narrow-band H α and UV imaging of NGC 3741 was obtained as part of the 11 Mpc H α and Ultraviolet Galaxy Survey (11HUGS; Lee et al. 2007; Kennicutt et al. 2008). The star formation rate (SFR) estimates derived from the H α and FUV luminosities are, respectively, $3.6 \times 10^{-3} M_{\odot} \text{ yr}^{-1}$ and $4.9 \times 10^{-3} M_{\odot} \text{ yr}^{-1}$ (Begum et al. 2008; Karachentsev & Kaisina 2013), in agreement with the SFR derived from CMDs of resolved stellar populations (Weisz et al. 2011; Johnson et al. 2013). The SFR and gas surface densities averaged within the stellar disc are compatible with the Kennicutt–Schmidt and extended Schmidt laws for spirals and dIrr galaxies (Talbot & Arnett 1975; Dopita & Ryder 1994; Begum et al. 2008; Roychowdhury et al. 2015, 2017). Most of the H α emission is confined within a central region of $\sim 12\text{-arcsec}$ radius ($\sim 0.19 \text{ kpc}$), where the azimuthally averaged H I column density is $N_{\text{HI}} \gtrsim 1.7 \times 10^{21} \text{ cm}^{-2}$ ($\sim 13.6 M_{\odot} \text{ pc}^{-2}$; Begum et al. 2008). However, the FUV emission extends to a larger galactocentric distance of $\approx 120 \text{ arcsec}$ or $\approx 1.9 \text{ kpc}$ (see e.g. Roychowdhury et al. 2017), suggesting that star formation occurred within the last $\sim 100 \text{ Myr}$ also in regions of the H I disc which are farther from the

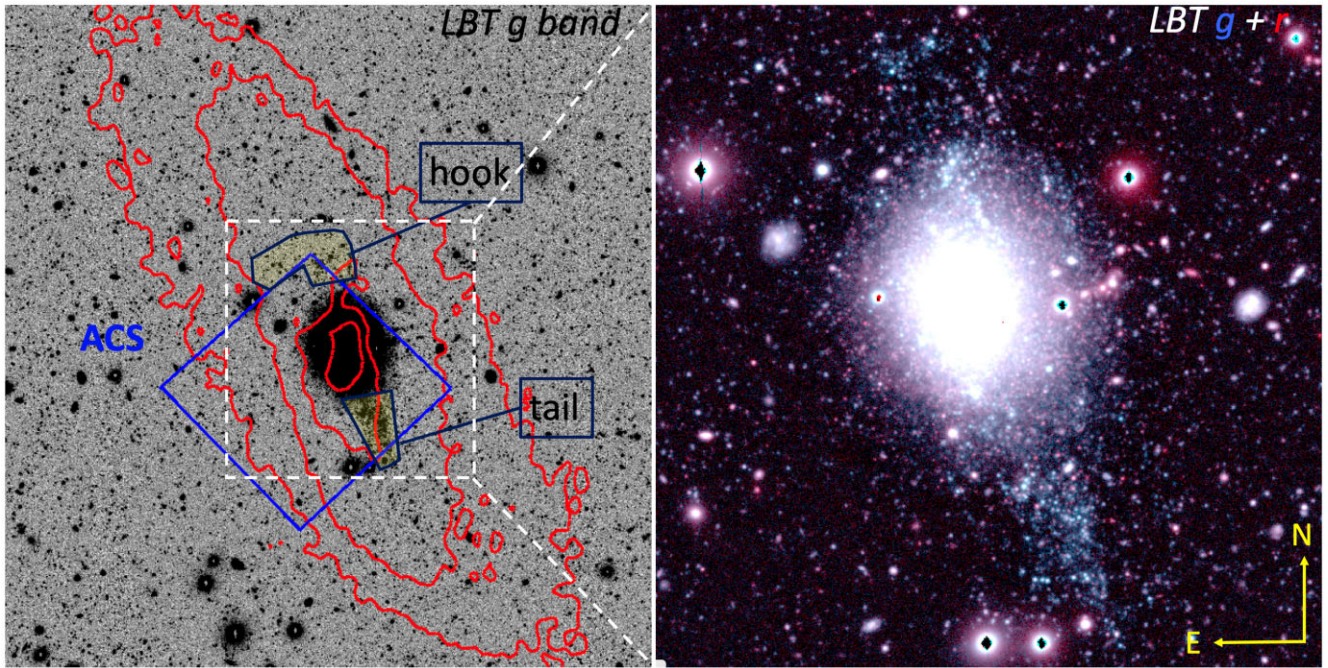


Figure 1. Left-hand panel: portion of the LBC g image of NGC 3741 with a field of view of $\sim 11 \times 11$ arcmin 2 , or $\sim 10 \times 10$ kpc 2 at the galaxy distance of ~ 3.2 Mpc. The polygons to the NE and SW of the galaxy enclose the newly identified features, dubbed the ‘hook’ and the ‘tail’ in this paper. The ACS footprint of archival observations includes the whole tail and a portion of the hook. For comparison, we also show in red the contours at 0.5, 3, 8, and 15 $M_{\odot} \text{pc}^{-2}$ of the H I total intensity map from the same WSRT data used in Gentile et al. (2007). Right-hand panel: g and r colour-combined image of NGC 3741 with a smaller field of view of $\sim 4 \times 4$ arcmin 2 corresponding to the dashed square in left-hand panel.

galaxy centre. NGC 3741 was also observed with Spitzer in the mid-(MIR) and far-infrared (FIR) as part of the Spitzer Local Volume Legacy Survey (Dale et al. 2009). From FUV-to-FIR spectral energy distribution fitting, Cook et al. (2014) derived a low internal dust extinction of $A_{\text{FUV}} = 0.047$ mag, in agreement with the observed trend of lower mass galaxies being less opaque than more massive ones. From spectroscopic observations of H II regions, Berg et al. (2012) measured an oxygen abundance of $12 + \log(\text{O}/\text{H}) = 7.68 \pm 0.03$ (i.e. $\sim 1/12$ solar metallicity), implying that NGC 3741 fits within the stellar mass-metallicity relation defined by dwarf galaxies (e.g. Berg et al. 2012; Pustilnik, Perepelitsyna & Kniazev 2016).

In this paper, we aim to understand the origin of the peculiar properties of NGC 3741 by comparing the stellar and the gas components of the galaxy. In Section 2, we present the new LBT images for NGC 3741 and analyse the stellar populations using both LBT and archival *Hubble Space Telescope* (*HST*) photometry. In Section 3, we use archival 21-cm observations to study the distribution and kinematics of the neutral gas. Section 4 provides a comparison between the properties of the stellar populations and the gas component and a discussion of the possible formation scenarios for NGC 3741. We give our summary in section 5.

2 STELLAR POPULATIONS

In this section, we analyse LBT and *HST* photometric data of NGC 3741 in order to derive the age and spatial distribution of the stellar populations using resolved-star CMDs.

2.1 LBT data

NGC 3741 was observed with the LBC on the LBT in the g and r bands as part of the SSH survey (Annibali et al. 2020, hereafter

Paper I). The left-hand panel in Fig. 1 shows a 11×11 arcmin 2 portion of the larger 25×25 arcmin 2 imaged field of view, with superimposed the H I contours from the same WSRT data used in Gentile et al. (2007). Our deep LBC data reveal the presence of two prominent blue stellar features extending in the direction of the galaxy major axis. These features are well visible in the 4×4 arcmin 2 g, r colour-combined image insertion displayed in the right-hand panel of Fig. 1: a southern triangle-shaped tail and a northern hook. The southern tail, which extends for ~ 1 arcmin (or ~ 0.9 kpc at NGC 3741’s distance), is aligned with the direction of the central H I high-density contour but is slightly offset to the west, as we show in more detail in Section 4.1.

Photometry of individual sources was performed independently on the stacked mosaic g and r images using PSFEX (Bertin & Arnouts 1996) and then the two catalogues were matched in coordinates and combined together. Selection cuts based on the SEXTRACTOR *quality* flag were applied for a first removal of spurious and badly measured objects in the photometric catalogue. Then, we used diagnostics based on the comparison between aperture and point spread function fitting magnitudes to remove very extended sources, likely background galaxies, as described in details in Paper I.

The $r, g - r$ CMD for sources measured within a 11×11 arcmin 2 region centered on NGC 3741 is shown in Fig. 2. For comparison, the PARSEC stellar isochrones (Bressan et al. 2012), shifted to a distance of 3.2 Mpc and corrected for a foreground extinction of $E(B - V) = 0.02$ (Schlafly & Finkbeiner 2011), have been overplotted on the CMD. The displayed models cover a wide range in stellar ages, from 10 Myr up to 10 Gyr old. The isochrone metallicity is $Z = 0.001$, which is consistent with the value expected from the oxygen abundance of the ionized gas measured by Berg et al. (2012). The CMD is heavily contaminated by background galaxies and foreground Milky Way disc and halo stars: the former mainly

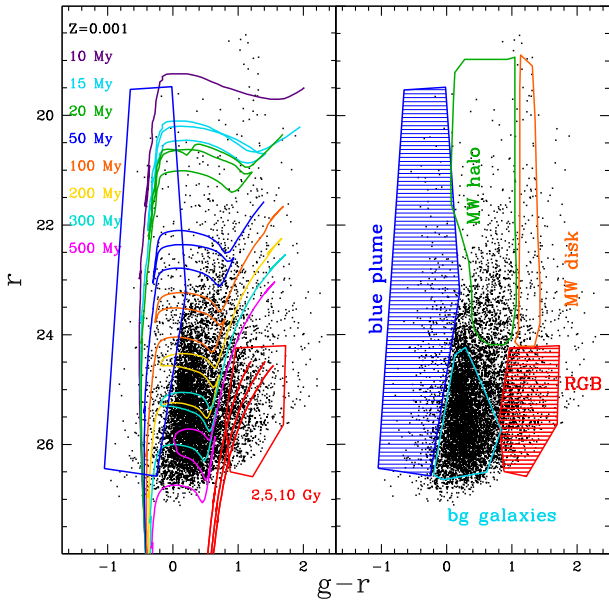


Figure 2. $r, g - r$ LBT CMD for sources within a 11×11 arcmin² region centered on NGC 3741. Superimposed on the left CMD are the PARSEC stellar isochrones (Bressan et al. 2012) in the SDSS photometric system, shifted to a distance of 3.2 Mpc and corrected for a foreground extinction of $E(B - V) = 0.02$ from Schlafly & Finkbeiner (2011). The displayed ages are in the range 10 Myr–10 Gyr and the metallicity is $Z = 0.001$, consistent with the H II spectroscopic metallicity of $12 + \log(O/H) = 7.68 \pm 0.03$ from Berg et al. (2012). The polygons indicate our selection of young (age ≤ 300 Myr) ‘blue plume’ stars and old (age > 1 –2 Gyr) RGB stars in NGC 3741, although some contamination from background galaxies remains. Highlighted on the right CMD are also the regions where background galaxies, and MW halo and disc stars tend to cluster.

populate the area indicated by the cyan contours in the right-hand panel at $-0.2 \leq g - r \leq 0.8$, $r \gtrsim 24$, while the latter dominate the CMD region at $g - r \gtrsim 0.2$, $r < 24$ shown by the green and orange contours. As described in Paper I, it is possible to partially separate stars belonging to NGC 3741 from foreground stars and background galaxies by selecting on the CMD the ‘blue plume’ at $g - r < 0$ populated by young stars (age ≤ 300 Myr) in the main sequence (MS) and blue core He-burning phases, and the RGB feature at $g - r \gtrsim 0.8$, $r > 24$ due to old (age > 1 –2 Gyr) low-mass stars.

Fig. 3 shows the spatial distribution of stars with different ages selected from the CMD. In the left-hand panel, we plot the density of old, RGB stars (age > 1 –2 Gyr) for a $\sim 11 \times 11$ arcmin² LBC region. The map was obtained by subtracting the average background computed in an external field and setting to zero all pixels below a level of three times the background standard deviation. This procedure allows us to mask density fluctuations due to the unresolved background galaxies (visible in the non-masked total map in the right-hand panel) not removed in our CMD selection. The result is a roundish, old stellar component; notice that the apparent lack of objects in the crowded galaxy centre is an artefact of the severe incompleteness at the faintest magnitudes and must not be interpreted as a real absence of old stars in the innermost regions of NGC 3741. Bright young stars are instead detected in the galaxy centre and extend beyond the old stellar component, following an elongated feature aligned in the direction of the H I disc major axis. This is an unusual property for dIrr and blue compact dwarf (BCD) galaxies, where irregular, extended, or filamentary structures

of young or intermediate-age stars are commonly present but do not encompass the old spheroid distribution (see e.g. Tosi et al. 2001; Momany et al. 2002; Annibali et al. 2008; Tolstoy, Hill & Tosi 2009; Annibali et al. 2013; Higgs et al. 2016; Sacchi et al. 2016; Cignoni et al. 2019; Annibali et al. 2020)

2.2 HST data

We searched the *HST* public MAST archive¹ for imaging data of NGC 3741. The deepest data are those acquired with the Advanced Camera for Survey (ACS) in the F475W ($\sim B$) and F814W ($\sim I$) filters as part of the ACS Nearby Galaxy Survey Treasury (ANGST; Dalcanton et al. 2009). The calibrated photometric catalogue was downloaded from the ANGRRR Photometry Repository.² The left-hand panel in Fig. 1 shows the ACS Wide Field Camera footprint superimposed to our LBC image. The ACS pointing includes almost the entire southern tail, but it samples just a portion of the northern hook.

The deep ACS I, $B - I$ CMD for well photometric point-like sources (i.e. selected to have a Dolphot (Dolphin 2000) flag = 0 and $|\text{sharpness}| \leq 0.07$) is shown in Fig. 4. Thanks to the high-spatial resolution and depth of the ACS data, the MS and blue core-He burning phases of stars with masses $\gtrsim 3 M_{\odot}$ are well-separated in these CMDs. This allows for a finer age separation of the different stellar populations than with the LBT data. More specifically, we identify five regions in the CMD that correspond to different age intervals:

- (i) the MS phase at $B - I \lesssim -0.2$ populated by stars younger than ~ 200 Myr;
- (ii) a bright portion of the MS (upper MS) at $I \lesssim 25$ populated by stars younger than ~ 50 Myr;
- (iii) the blue and red core He-burning (HeB) phases of massive and intermediate-mass stars with ages in the range 20–600 Myr;
- (iv) the brightest portion of the red clump (RC) at $B - I \sim 1.2$ and $26 \leq I \leq 26.5$ populated by HeB stars with ages of $\sim 0.8 - 1$ Gyr;
- (v) a bright portion of the RGB, down to ~ 2 mag below the tip, which allows us to isolate stars older than 1–2 Gyr.

Fig. 5 shows density maps for the spatial distribution of stars in these different ages bins, although some contamination from background galaxies can not be excluded also in this case. The ACS data confirm the presence of a smooth and round-shaped distribution for the old ($\gtrsim 2$ Gyr) stellar component, in agreement with the LBT data (sect. 2.1) and with the distribution of the 3.6- μm emission (Fig. 6), which is a good tracer of the old stellar population. In Appendix A, we show that the old star counts are fitted with a Sersic-profile component with index $m \sim 1.2$, effective radius $R_e \sim 20$ arcsec or ~ 0.31 kpc (see also value by Lelli et al. 2016, from the 3.6- μm band) and $M_g \sim -12.5 \pm 0.5$, consistent with scaling relations derived for dwarf spheroidal galaxies (e.g. Côté et al. 2008; Chen et al. 2010; Eigenthaler et al. 2018). On the other hand, very young stars (< 50 Myr) are concentrated within a central, ~ 0.4 kpc diameter region, as also outlined by the H α image from Kennicutt et al. (2008) shown in Fig. 6. Stars with ages between ~ 20 and ~ 600 Myr, and up to perhaps ~ 1 Gyr old, present an elongated distribution and populate both the southern tail and the portion of the northern hook covered by the ACS field of view, confirming the results from the

¹<https://archive.stsci.edu/>

²<https://archive.stsci.edu/prepds/angrrr/datalist.html> (J. Dalcanton, K. Gilbert, and B. Williams)

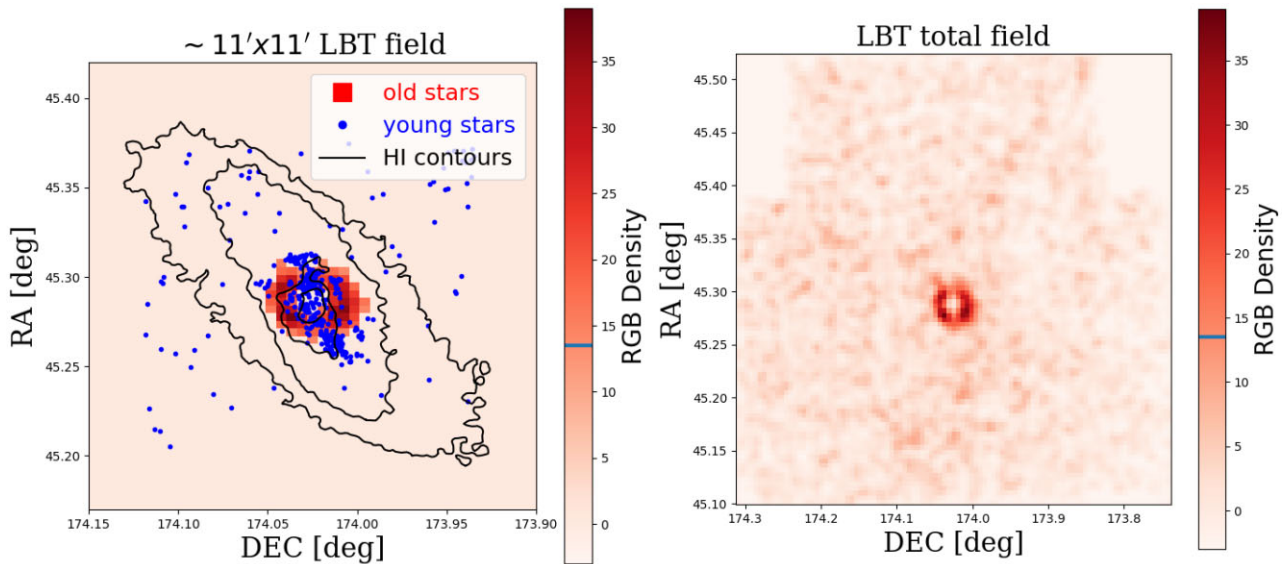


Figure 3. Spatial distribution of stars in NGC 3741 from LBT photometry. The left-hand panel shows the density of old, RGB stars (age $> 1\text{--}2$ Gyr) for a 11×11 arcmin² LBC region. The map is background-subtracted, and only pixels above a level of three times the background standard deviation (given by the horizontal blue segment in the colourbar) have been set to non-zero to mask density peaks due to red background galaxies. Blue dots are stars younger than $\lesssim 300$ Myr, while the solid HI contours are the same as in Fig. 1. The RGB density map for the total LBC field of view, with no pixel masking, is shown in the right-hand panel to provide a direct visualization of the contamination from red background galaxies.

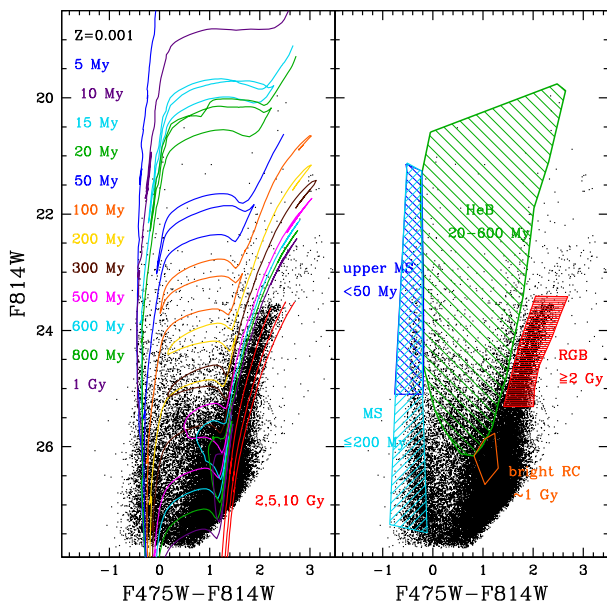


Figure 4. F814W ($\sim I$ -band) versus F475W-F814W ($\sim B-I$) CMD from the ACS data. In the left-hand panel, the PARSEC stellar isochrones (Bressan et al. 2012) in the ACS Vegamag photometric system, shifted to a distance of 3.2 Mpc and corrected for a foreground reddening of $E(B-V) = 0.02$, have been superimposed to the CMD. The models cover an age range from 5 Myr to 10 Gyr, as indicated in the legend, and the metallicity is $Z = 0.001$. In the right-hand panel, we highlight the five selected regions with stars in different age intervals: the MS phase with stars younger than ~ 200 Myr; the upper MS at $I \lesssim 25$ with stars younger than ~ 50 Myr; the blue and red core He-burning (HeB) phases of massive and intermediate-mass stars with ages in the range 20–600 Myr; the brightest portion of the red clump with ages of $\sim 0.8\text{--}1$ Gyr; a bright portion of the RGB tip with stars older than 1–2 Gyr.

LBT data. In particular, stars younger than ~ 200 Myr, which are very well-sampled by the MS phase in the ACS CMD, exhibit a bar-like structure from which the tail and the hook appear to depart. Also the distributions of the FUV emission and NUV emission, which respectively trace stars younger than 100 and 200 Myr (see Kennicutt & Evans 2012 and reference therein) resemble this ‘bar plus arms’ configuration. Spiral galaxies often host a bar and spiral arms, making NGC 3741 a sort of ‘young spiral galaxy’, but with two important differences. The first is, of course, the stellar mass of NGC 3741, which is much lower than the typical stellar mass of spiral galaxies. The second difference is that bars in spiral galaxies are typically made of old stars.

3 HI DISTRIBUTION AND KINEMATICS

We analysed the HI distribution and kinematics of NGC 3741 using the same 21-cm observations as Gentile et al. (2007), which were obtained with the WSRT (Tom Oosterloo, private communication). Because of minor differences in the data reduction, this data cube has velocity resolution of 4.1 km s^{-1} , the same as Gentile et al. (2007), but the beam size is $18.9 \times 13.8 \text{ arcsec}^2$, which is slightly lower spatial resolution than their highest-resolution cube.³

In our study, we used the software ^{3D}BAROLO⁴ (Di Teodoro & Fraternali 2015), which performs a tilted-ring model fitting directly on the data cube. This software models the galaxy emission by dividing the galactic disc into a series of concentric and co-planar rings with a given width. Each ring is described by four geometric parameters (i.e. the two centre coordinates, the inclination with respect to the line of sight i , and the position angle PA) and four kinematic parameters (i.e. the systemic velocity of the galaxy V_{sys} , the rotation velocity of

³We did also try to use the publicly available 21-cm data cubes from the survey VLA-ANGST (Ott et al. 2012), but we abandoned them, because we found several and relatively bright artifacts in the channels.

⁴<https://editeodoro.github.io/Bbarolo/>

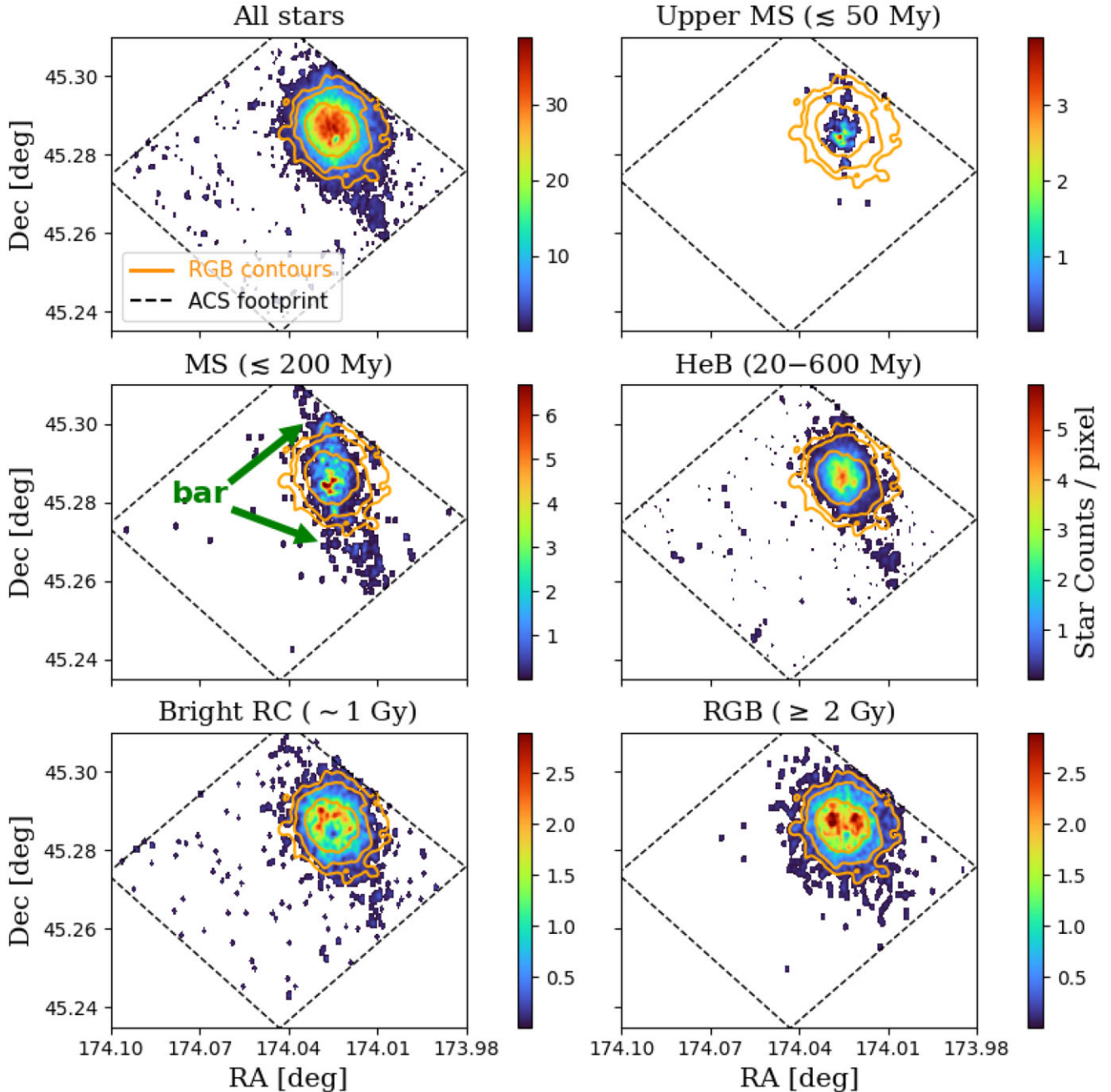


Figure 5. Stellar density maps for sources in the ACS catalogue. The left-hand upper panel shows the map for the totality of measured stars, while the other panels refer to stars in different age intervals according to the CMD-based selection of Fig. 4: stars younger than ~ 50 Myr, younger than ~ 200 Myr, with ages in the 20–600 Myr range, with ages of ~ 1 Gyr, and older than ~ 2 Gyr. The contours for the old, RGB population are superimposed for reference to all spatial maps. The dashed line denotes the ACS footprint. The identified stellar bar-like structure is indicated in the panel for ages $\lesssim 200$ Myr.

the gas in circular orbits V_{rot} , the gas velocity dispersion σ_{H1} , and the radial velocity of the gas with non-circular motions V_{rad}). This model is iteratively fitted to the data cube in order to find the set of free parameters that minimizes the residuals between the model and the observations. Prior to the residuals minimization, $^3\text{D}\text{BAROLO}$ smooths the galaxy model to the same resolution of the observations, allowing to take into account the beam smearing effect. It is worth to notice that, for each ring, $^3\text{D}\text{BAROLO}$ simultaneously fits the rotation velocity and the azimuthally averaged velocity dispersion. This markedly improves the reliability of velocity dispersion estimates with respect

to 2D methods (e.g. second-moment map of the data cube, stacking or pixel-by-pixel fitting of the line profiles) also for data with low signal-to-noise ratio (S/N).

For our modelling with $^3\text{D}\text{BAROLO}$, we assumed a distance of 3.2 Mpc, $V_{\text{sys}} = 229 \text{ km s}^{-1}$ and the kinematic centre at (RA: $11^{\text{h}}36^{\text{m}}6^{\text{s}}.20$; Dec.: $45^{\text{d}}17^{\text{m}}4.00\text{s}$), which are fully compatible with the values reported in the literature (Gentile et al. 2007; Ott et al. 2012). Prior to the model fitting, $^3\text{D}\text{BAROLO}$ creates a mask and applies it to the data cube in order to isolate the galaxy emission. We created the mask by smoothing the data cube to a factor 2 lower resolution

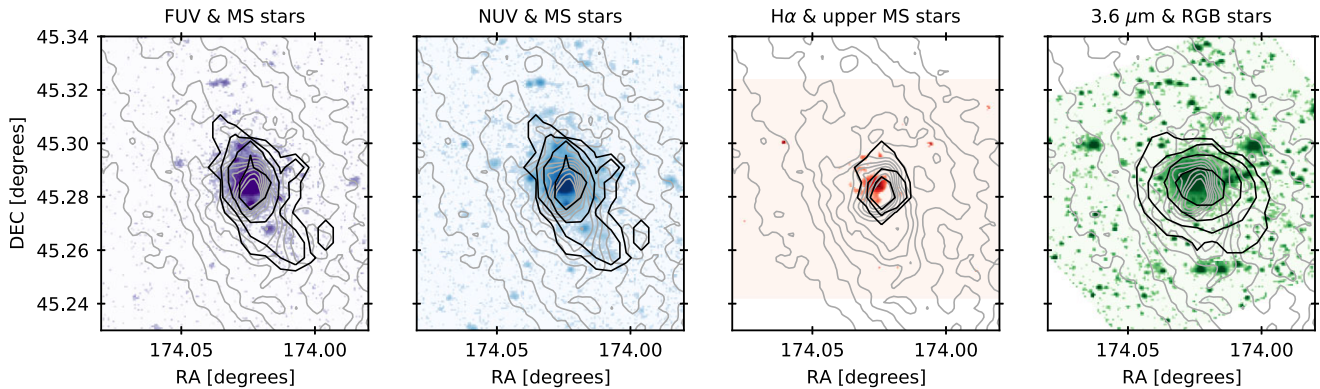


Figure 6. Archival observations of NGC 3741: from left- to right-hand panel, the panels show the FUV emission and the NUV emission observed with *GALEX* (Lee et al. 2007), the $H\alpha$ emission (Kennicutt et al. 2008), and the $3.6\ \mu\text{m}$ emission observed with *Spitzer* (Dale et al. 2009). The solid black contours indicate the distribution of different stellar populations selected from the *HST* CMD: MS stars with ages $\lesssim 200$ Myr (first and second panels from the left), bright MS stars with ages $\lesssim 50$ Myr (third panel), and RGB stars with ages > 2 Gyr (fourth panel from left). The black contours are at 2^k number of enclosed stars with $k = 1, 3, 5, \dots, 19$. The light grey contours are the H I iso-density contours (see Section 3), starting from $1\ M_{\odot}\ \text{pc}^{-2}$ and increasing with steps of $2\ M_{\odot}\ \text{pc}^{-2}$.

and selecting only the pixels with $S/N > 3$ in this low-resolution cube. This procedure allows us to include also the faint galactic emission in the masked cube used for modelling the H I kinematics.

Fig. 7 shows the total intensity map and the velocity field obtained from the masked data cube. From the total intensity map in the left-hand panel, we can see that the H I disc has two evident properties: (i) the H I surface density is very high in the innermost regions, where $\Sigma_{\text{H I}} \gtrsim 26\ M_{\odot}\ \text{pc}^{-2}$, and (ii) inside the H I disc, two spiral arm-like structures seem to propagate from the galaxy centre (see also Gentile et al. 2007). From the velocity field in the right-hand panel, we see that the kinematic major axis ($\text{PA} \simeq 45^\circ$), which connects the regions with extreme line-of-sight velocities (V_{LOS}), does not coincide with the geometric major axis ($\text{PA} \simeq 34^\circ$). Together with the distorted iso-velocity contours, this suggests the presence of a warp. We note that the offset between the systemic velocity and the line-of-sight velocity along the minor axis is also a signature of radial motions (e.g. Fraternali et al. 2002; Lelli et al. 2012b; Di Teodoro & Peek 2021), which might be ascribed to the presence of a bar, ongoing gas accretion, or an oval distortion of the gravitational potential (e.g. Bosma 1978, 1981; Kormendy & Kennicutt 2004).

To run $^3\text{D}\text{BAROLO}$, we fixed the width and the scale height of the rings at 15 arcsec and 10 arcsec, respectively.⁵ Following Gentile et al. (2007), the galaxy inclination was fixed at $i = 70^\circ$ for all the rings. We allowed $^3\text{D}\text{Barolo}$ to correct for the asymmetric drift (Oh et al. 2015; Iorio et al. 2017), even though the pressure support against gravity is negligible with respect to the rotational support for NGC 3741 (Gentile et al. 2007).

Since radial motions are degenerate with the viewing angles (Schoenmakers, Franx & de Zeeuw 1997; Schoenmakers 1999), it is not advisable to fit both the PA and V_{rad} at the same time. Hence, we first run $^3\text{D}\text{BAROLO}$ assuming $V_{\text{rad}} = 0\ \text{km}\ \text{s}^{-1}$, and fitting

⁵ $^3\text{D}\text{Barolo}$ is insensitive to the scale height as the tilted-ring fitting procedure is done ring-by-ring. For a thick disc, one line of sight can intersect emission from different annuli because of the projection effects due to the disc inclination. By studying the H I kinematics of dwarf galaxies, Iorio et al. (2017) found that assuming a constant scale height does not significantly affect the best-fitting kinematical parameters, since any difference is smaller than the associated uncertainties. A value smaller than the beam is therefore a conservative choice for the scale height.

V_{rot} , $\sigma_{\text{H I}}$, and PA.⁶ The comparison between the best-fitting model and the observations is provided in the left-hand panels of Fig. 8. From the pv-diagram along the major axis (upper left-hand panel in Fig. 8), we see that our model reproduces fairly well the H I emission. However, we notice some discrepancy in the pv-diagram along the minor axis (lower left-hand panel in Fig. 8): although the contours of the model emission grossly reproduce the observations, there are regions (indicated by the green arrows) where the H I emission is more extended than the model contours, suggesting the presence of gas with anomalous kinematics. In Appendix B, we show the rotation curve, the velocity dispersion radial profile and the azimuthally averaged radial profile of the H I surface density obtained for this first best-fitting model.

We then built a second model by fixing the PA at 34° based on the morphological major axis, and fitting V_{rot} , $\sigma_{\text{H I}}$, and V_{rad} (central panels, Fig. 8). Compared to the previous case, the inclusion of radial motions improves the modelling of the H I emission in the pv-diagram along the minor axis, as indicated by the green arrows. The extent of the observed emission is well reproduced by the model. The radial profiles of V_{rot} , $\sigma_{\text{H I}}$, and $\Sigma_{\text{H I}}$ of this second model are compatible within the uncertainties with those obtained for the first model (see Appendix B).

We also obtained a third best-fitting model by fixing V_{rad} and fitting V_{rot} , $\sigma_{\text{H I}}$, and PA in order to include both the warp and radial motions. After various trials with different values of V_{rad} , we obtained a satisfactory fit assuming $V_{\text{rad}} = -5\ \text{km}\ \text{s}^{-1}$ (see the right-hand panels of Fig. 8), which is consistent with the results of Gentile et al. (2007). This model reproduces fairly well the H I emission and, in particular, it is able to account for the H I with anomalous kinematics indicated by the green arrows in the pv-diagram along the minor axis. From a channel-by-channel inspection, we conclude that the second model with radial motions but no warp and the third model with both the warp and radial motions are equally good at reproducing the observations. The rotation curve and the radial profiles of $\sigma_{\text{H I}}$ and

⁶In order to avoid unrealistic discontinuities, we regularized the PA radial profile by choosing the two-step fitting procedure of $^3\text{D}\text{BAROLO}$ (`twostage = True`): after the first run, the PA profile is interpolated using a second-order polynomial function, which is then used in the second run to remove a free parameter from the fit.

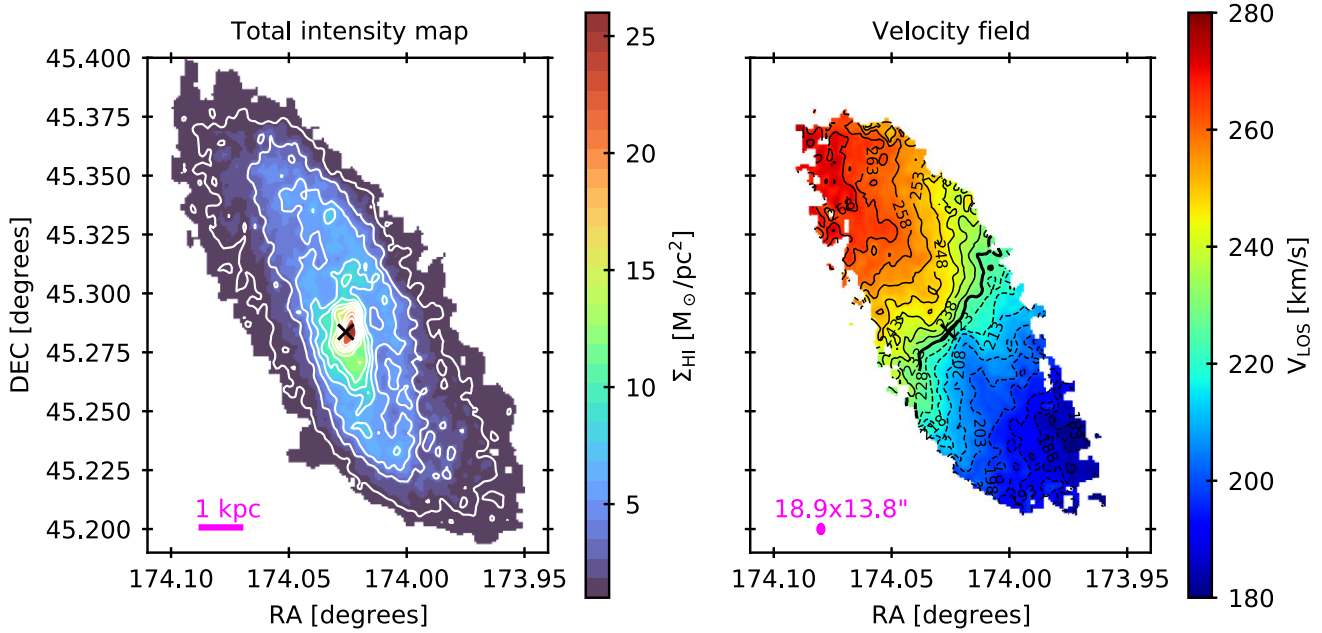


Figure 7. Left-hand panel: H I total intensity map from WSRT observations. The white contours are the iso-density curves, which start at $1 M_{\odot} \text{pc}^{-2}$ (roughly corresponding to the 3σ pseudo noise level in the total map; see Verheijen & Sancisi 2001; Lelli, Verheijen & Fraternali 2014c) and increase with steps of $2 M_{\odot} \text{pc}^{-2}$ up to $21 M_{\odot} \text{pc}^{-2}$. The magenta bar shows the physical scale of the observations. Right-hand panel: velocity field (only pixels with $\Sigma_{\text{HI}} > 1 M_{\odot} \text{pc}^{-2}$ are shown). The black curves are the iso-velocity contours spaced by $\pm 5 \text{ km s}^{-1}$ from $V_{\text{sys}} = 228 \text{ km s}^{-1}$ (thick contour). Solid and dashed curves are, respectively, for the receding side and the approaching side of the disc. The magenta dot shows the beam size. In both panels, the black cross indicates the kinematic centre.

Σ_{HI} of this third model are compatible with those of the previous models (see Appendix B).

We note that these estimates of V_{rad} can be very uncertain, since the superimposition of emission at different line-of-sight velocities can influence the determination of V_{rad} . This issue might be important in the case of galaxies with a warp along the line of sight and for significantly thick gas discs, which is likely the case of dwarf galaxies (e.g. Roychowdhury et al. 2010; Iorio et al. 2017; Bacchini et al. 2020; Patra 2020). Since it is not known which side of the disc is the closest to the observer, it is not possible to unambiguously discern between gas inflow or outflow, hence the sign of derived V_{rad} is also uncertain. If we assume that the H I spiral arms are trailing with respect to the rotation direction, we can infer that the galaxy is rotating clockwise and that the gas is inflowing with a median mass inflow rate of the order of $0.1 M_{\odot} \text{yr}^{-1}$, in agreement with the most recent estimates for star-forming galaxies in the local Universe (see Di Teodoro & Peek 2021).

4 DISCUSSION

In this section, we first compare the results obtained from the analysis of the stellar and the gaseous components. Then, we discuss possible evolution scenarios that can explain the peculiar properties observed in NGC 3741.

4.1 Comparison between stars and gas

In Fig. 9, we compare the distribution of the stellar populations with different ages (see Section 2) with the H I distribution and kinematics (see Section 3), focusing on a $7 \times 7 \text{ arcmin}^2$ central galaxy region. The figure immediately emphasizes the significantly smaller spatial extension of the stellar components compared to the H I.

The bulk of the youngest stars (age $\lesssim 50 \text{ Myr}$) is concentrated within a central region of $\lesssim 1 \text{ kpc}$ size and coincides with the highest density peak in the H I emission at $\Sigma_{\text{HI}} \simeq 26 M_{\odot} \text{pc}^{-2}$. On the other hand, the bar-like structure, the ‘northern hook’ and the ‘southern tail’ ($\lesssim 300 \text{ Myr}$ old) are aligned along the direction of the H I disc major axis and are about three times more spatially extended than the youngest stellar population. The bar coincides with the high H I density region suggested in previous studies to be a purely gaseous bar (e.g. Begum et al. 2005; Gentile et al. 2007; Banerjee et al. 2013). The hook and the tail appear slightly (anti-clockwise) rotated with respect to the direction of the H I spiral arms emanating from the galaxy centre. We notice that the tail is located at the same position of the strong distortion in the H I iso-velocity contours at $208\text{--}213 \text{ km s}^{-1}$.

The oldest (age $\gtrsim 2 \text{ Gyr}$) stellar population is also located at the centre of the H I disc, but its distribution is round and does not appear to follow the H I morphology. It encompasses regions with H I densities from $\simeq 26 M_{\odot} \text{pc}^{-2}$ down to $\simeq 6 M_{\odot} \text{pc}^{-2}$ with increasing galacto-centric distance. As discussed in Section 2, this old and spheroidal stellar component appears less spatially extended than the stars with age $\lesssim 200\text{--}300 \text{ Myr}$. This property is unusual for dIrrs, which often host extended or filamentary structures of young or intermediate-age stars, but these are typically less spatially extended than the old stellar component (see e.g. Tosi et al. 2001; Momany et al. 2002; Annibali et al. 2008, 2013, 2020; Tolstoy et al. 2009; Higgs et al. 2016; Sacchi et al. 2016; Cignoni et al. 2019).

4.2 NGC 3741, a dwarf spiral galaxy?

The properties of NGC 3741 – i.e. the presence of an extended, rotationally supported H I disc, H I spiral arms, an old spheroidal stellar component, and extended younger stellar structures – could

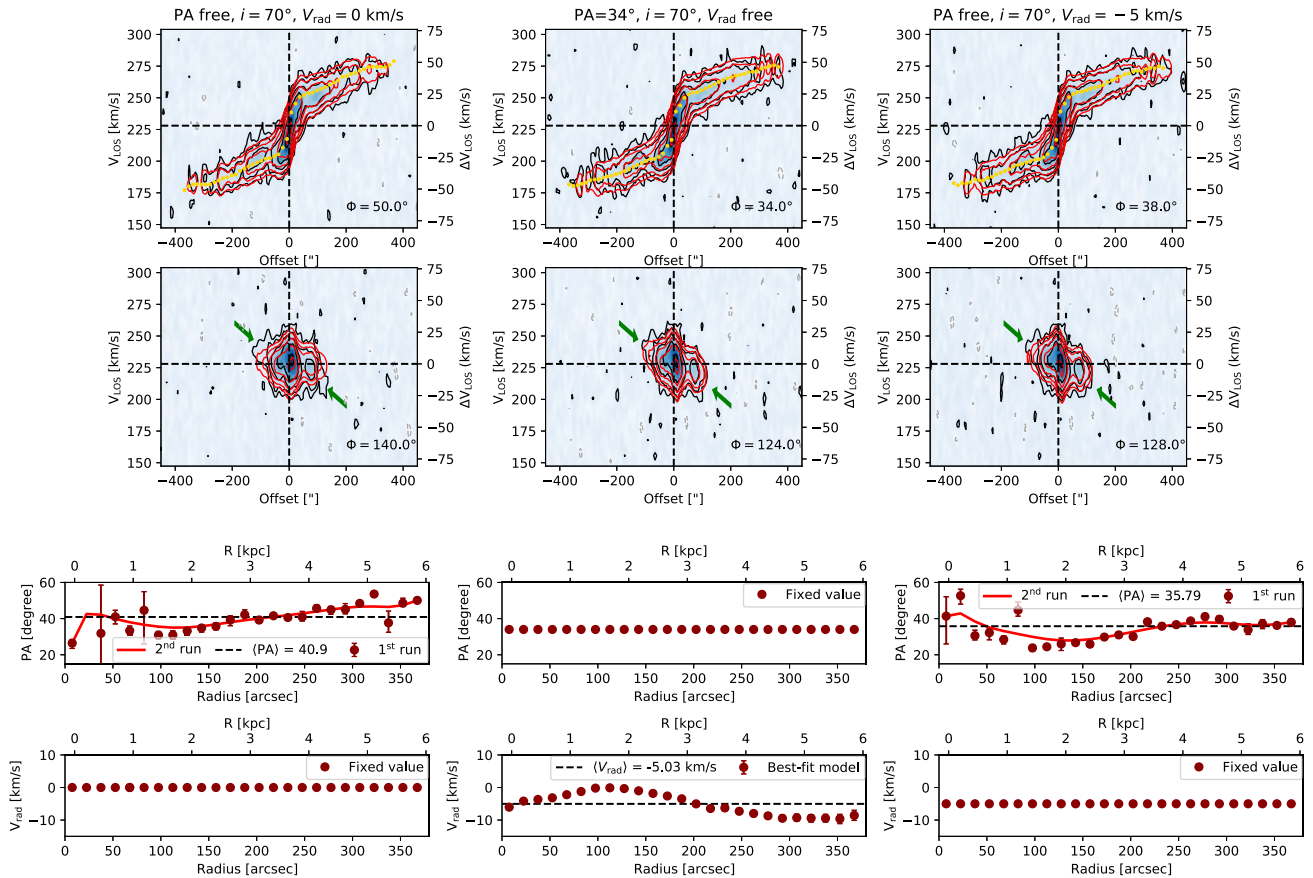
NGC3741: ^{3D}Barolo models vs observations


Figure 8. Comparison between the H I observations and three best-fitting models obtained with ^{3D}BAROLO using, for each column, different sets of parameters (see text for details). *First and second rows:* pv-diagram along the kinematic major and minor axes, respectively (notice that, depending on the best-fitting model, the pv-diagrams are for different axis orientations, which are indicated by Φ in each panel); the observed H I emission is shown in blue (the black contours are at $2.5 \times \sigma_{\text{ch}} \times 2^n$, with $\sigma_{\text{ch}} = 1.39 \text{ mJy beam}^{-1}$ being the noise in the data cube channels), while the model emission is shown by the red contours. The yellow points in the first row panels trace the rotation curve of the best-fitting models. The green arrows in the second row panels indicate the emission at velocities compatible with non-circular motions. *Third and fourth rows:* PA and the radial velocity as a function of the galactocentric radius R for the best-fitting models. The red points show either the best-fitting parameters or the assumed values, while the red curves, when present, are the regularized profiles. The black dashed line indicates the median of the free parameters.

suggest that we are observing a low-luminosity spiral galaxy with a prominent bulge and faint spiral arms. Indeed, NGC 3741’s stellar mass of $3.8 \times 10^7 M_{\odot}$ is about one order of magnitude lower than the stellar mass of the smallest known spiral galaxies (see e.g. the compilation in Calzetti et al. 2015), which would make this system a rare, extremely low-mass spiral galaxy. Dwarf galaxies are known to typically lack strong spiral structures, even in the presence of an extended, gaseous disc dominating the baryonic component. Ghosh & Jog (2018) suggest that in these systems, the dark halo tends to suppress the growth of non-axisymmetric perturbations in the gas components and that only occasional, weak spiral features (such as those observed in the H I disc of NGC 3741) can be triggered by tidal encounters or by gas accretion.

4.3 A gaseous and stellar bar in NGC 3741?

Previous authors (Begum et al. 2005, 2008; Gentile et al. 2007; Banerjee et al. 2013) ascribed the presence of radial motions in NGC 3741 to a purely gaseous bar, which can be tentatively identified

as a central and elongated region with high H I density (see left-hand panel in Fig. 7). However, purely gaseous bars are rarely observed: besides NGC 3741, the only other known cases are those of DDO 168 (Patra & Jog 2019) and NGC 2915 (Bureau et al. 1999). Indeed, the elongated, bar-like structure made of intermediate-age stars ($\lesssim 200\text{--}300 \text{ Myr}$) in the top right- and bottom right-hand panels of Fig. 9 may be the stellar counterpart of the gaseous bar previously detected in NGC 3741. However, a bar is not identified in the stellar population older than 2 Gyr, which constitutes more than 80 percent of the total stellar mass of NGC 3741 (Weisz et al. 2011) and exhibits a spheroidal distribution.

Stellar bars are thought to typically form as a consequence of disc instability (e.g. see Athanassoula 2013, for a review) but several studies have shown that a dominant dark matter halo tends to slow down bars (Debatista & Sellwood 1998) or even to prevent their formation (Mihos, McGaugh & de Blok 1997) in dwarf galaxies. Stellar and gaseous bars may also form as a consequence of tidal interactions (Gajda et al. 2018; Pettitt & Wadsley 2018) or gas accretion (Combes 2014). For instance, through N -body hydrodynamical

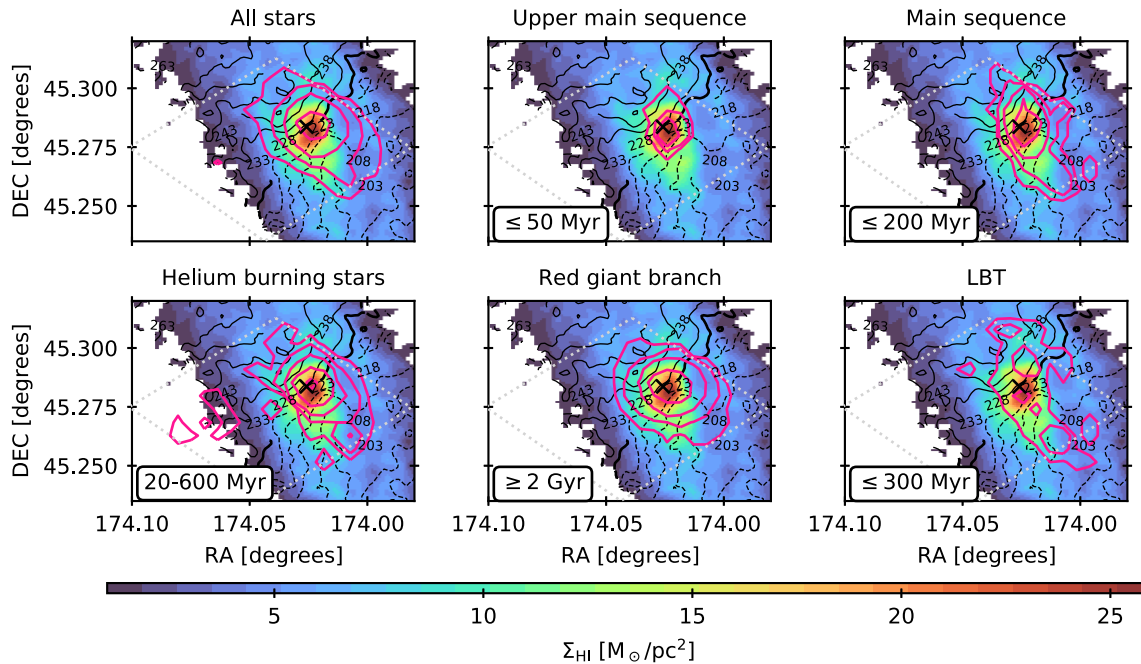


Figure 9. Comparison between the distribution of stars with different ages and the H I distribution and kinematics. The H I total intensity map is coloured according to the H I surface density in $M_{\odot} \text{pc}^{-2}$. The iso-velocity contours (in km s^{-1}) from the H I velocity field are shown by the solid and dashed lines for the approaching and the receding side, respectively; the thick contour indicates the systemic velocity. The grey box indicates the ACS FOV and the magenta contours show the distribution of stars (we note that the different box shape from Fig. 5 is due to the different scale). Top left-hand panel: distribution of all the stars from ACS data. Other panels: distribution of stars in different age bins, as indicated by boxes in the bottom left-hand corner of the panels. The bottom right-hand panel is obtained using the LBT observations.

simulations, Gajda et al. (2018) showed that stellar bars can be tidally induced by encounters with a massive host in dwarf galaxies that would otherwise be stable against bar formation for several Gyrs. The hypothesis of a tidally induced bar in NGC 3741 is appealing also because of the relatively young ages of the stars organized in the elongated, bar-like structure, suggesting that a putative interaction may have occurred just a few hundred Myr ago.

According to Marasco et al. (2018), weak stellar bars can also form in dwarf galaxies if the dark matter halo is triaxial; this would also induce non-circular motions in the gas component. However, in this scenario, it seems difficult to explain the absence of a bar-like feature in the old stellar component of NGC 3741.

4.4 NGC 3741, the precursor/descendant of a starburst dwarf galaxy?

The H I analysis presented in this paper shows that NGC 3741 has a very high H I density at its centre and that the rotation curve rises steeply in the inner regions, which are properties typical of BCD galaxies. BCDs, sometimes also called star-bursting dwarf galaxies, have higher central H I surface densities than ‘normal’ dIrrs and steeply rising rotation curves (e.g. van Zee, Skillman & Salzer 1998; Simpson & Gottesman 2000; Lelli, Verheijen & Fraternali 2014b). These properties indicate a strong mass concentration at their centre, suggesting that the starburst is closely related to the central shape of the gravitational potential and to the inner concentration of gas (van Zee, Salzer & Skillman 2001; Lelli et al. 2012a,b, 2014b; Lelli, Fraternali & Verheijen 2014a). Moreover, Lelli et al. (2014a) identified a population of ‘compact’ dIrrs with steeply rising circular velocities (similar to those of BCDs) but moderate star formation activity. These authors proposed that compact dIrrs are the best

candidates for being either the progenitors or the descendants of BCDs. NGC 3741, which shows all the typical characteristics of BCDs with the important exception of the SFR, may fit into this scenario, as discussed in the following.

The azimuthally averaged central H I surface density of NGC 3741 is $\approx 8 M_{\odot} \text{pc}^{-2}$ (see Appendix B) and its inner circular velocity gradient, defined as $V_c(R_d)/R_d$ (with R_d being the exponential disc scale length), is $\sim 50 \text{ km s}^{-1} \text{ kpc}^{-1}$; both these values are consistent with the typical values of BCDs and compact dIrrs (Lelli et al. 2014a). For comparison DDO 87, a dIrr with H I mass and maximum circular velocity similar to those of NGC 3741, has a much lower inner H I surface density of $\approx 3 M_{\odot} \text{pc}^{-2}$ and a lower inner velocity gradient of $\sim 22 \text{ km s}^{-1} \text{ kpc}^{-1}$. However, the average SFR surface density within the optical radius of NGC 3741 is $\Sigma_{\text{SFR}} \approx 4 \times 10^{-3} M_{\odot} \text{yr}^{-1} \text{ kpc}^{-2}$ (Lee et al. 2007; Begum et al. 2008; Kennicutt et al. 2008; Johnson et al. 2013; Roychowdhury et al. 2017), which is more typical of normal dIrrs rather than of strong starburst dwarfs (e.g. Tolstoy et al. 2009; Cignoni et al. 2019).

What is the origin of the peculiar properties observed in NGC 3741? We suggest that a merger event or gas accretion from the intergalactic medium may be the cause. In fact, the H I disc of NGC 3741 is about seven times more extended than the stellar component, a property observed only in few other dwarfs such as DDO 154 (e.g. Krumm & Burstein 1984; Iorio et al. 2017), NGC 4449 (Bajaja, Huchtmeier & Klein 1994; Lelli et al. 2014b), NGC 2915 (Meurer et al. 1996), and I Zw 18 (e.g. Lelli et al. 2012a, 2014b). It has been suggested that these extended H I discs may accumulate from the accretion of cold gas, either through minor mergers or from gaseous filaments coming from intergalactic medium (see Sancisi et al. 2008, and references therein). In NGC 3741, this scenario is supported by the possible existence of a symmetric warp and by the

presence of radial motions throughout the HI disc which seem to increase towards the galaxy outskirts. Under the assumption that the HI spiral arms are trailing with respect to the rotation direction, i.e. that the galaxy is rotating clockwise, the observed radial motions translate into an inflow of gas towards the galaxy centre.

The anomalous extended young stellar components, i.e. the ‘tail’, the ‘hook’, and the bar-like stellar structure (superimposed to a bar-like gaseous overdensity) seem to strengthen the accretion/merger hypothesis: these anomalous features may, in fact, originate from gas inflow towards the galaxy centre that has triggered star formation a few hundred Myr ago. However, the uncertainties in the derived SFH (Weisz et al. 2011) do not allow us to confirm or exclude the occurrence of a major starburst in NGC 3741 a few hundred Myr ago and to evaluate if its strength was comparable to those typically observed in BCDs. It is also possible that this galaxy is now at the beginning of a star-bursting phase and ready to turn into a BCD.

5 SUMMARY AND CONCLUSIONS

Our study shows that NGC 3741 exhibits peculiar properties for dwarf galaxies, both in its stellar and in its gas components. LBT and *HST* imaging revealed the presence of a bar-like stellar structure from which two elongated features, that we dub the ‘northern hook’ and the ‘southern tail’, appear to depart. This bar–hook–tail feature extends for ~ 3.5 kpc in the direction of the HI disc major axis, is dominated by stars a few hundred Myr old, and is about twice as extended as the old (age > 2 Gyr) stellar component. On the other hand, very young stars (age < 50 Myr) are confined to the central ($\lesssim 1$ kpc) region of the galaxy where the HI density is the highest. This configuration is quite uncommon among dwarf galaxies: (i) although irregular, extended, or filamentary structures made of very young-to-several hundred Myr old stars are often present there, such features do not typically encompass the spatial distribution of the old stellar component; (ii) since their potential is dominated by the dark matter halo, dwarf galaxies are thought to be quite stable against bar formation; (iii) a bar composed of young stars, but not identified in the old stellar component, is quite unusual and difficult to explain.

To investigate the origin of the peculiar stellar properties and their association with the gas, we performed a new analysis of HI archival data. The stellar bar coincides with a central, elongated region of high HI density suggested in previous studies to be a purely gaseous bar. The hook and the tail appear slightly (anti-clockwise) rotated with respect to the direction of the HI spiral arms emanating from the galaxy centre. From the HI kinematics, we confirm the presence of HI radial motions (indicating an inflow/outflow).

The HI distribution and kinematics indicate that the surface density is very high at the galaxy centre, peaking at $\simeq 26 M_{\odot} \text{pc}^{-2}$, and that the rotation curve rises steeply in the inner regions, indicating a strong concentration of mass at the galaxy centre. These properties are typical of star-bursting BCD galaxies, but less common for dIrr galaxies with modest SFRs, such as NGC 3741.

These results lead us to speculate that the unusual properties observed in NGC 3741 may be due to an advanced-stage merger with a low-mass companion or to the accretion of gas from the intergalactic medium, which caused the gas to inflow towards the central regions and triggered star formation a few hundred Myr ago, forming two elongated young stellar features (the ‘tail’ and the ‘hook’) and a central bar-like structure superimposed to a similarly elongated HI overdensity. This accretion/interaction event may also explain the presence of a very extended HI disc and of the central HI spiral arms. The high central HI density and the steeply rising

rotation curve suggest that NGC 3741 may be the progenitor or the descendant of a starburst dwarf.

ACKNOWLEDGEMENTS

We would like to thank Filippo Fraternali for the invaluable help with the data interpretation and fruitful discussions on the results, and Tom Oosterloo for providing the reduced WSRT data cube and helping with its interpretation. We are much indebted to the anonymous referee for his/her extremely useful comments and suggestions. We acknowledge the support from the LBT-Italian Coordination Facility for the execution of observations, data distribution, and reduction. MB, FA, MC, and MT acknowledge the financial support from INAF Main Stream grant 1.05.01.86.28 ‘SSH’. FA, MC, and MT acknowledge funding from INAF PRIN-SKA-2017 programme 1.05.01.88.04.

CB acknowledges the financial support from the European Research Council (ERC) under the European Union’s Horizon 2020 research and innovation programme (grant agreement no. 833824).

Based on data acquired using the LBT. The LBT is an international collaboration amongst institutions in the United States, Italy, and Germany. LBT Corporation partners are The University of Arizona on behalf of the Arizona university system; Istituto Nazionale di Astrofisica, Italy; LBT Beteiligungsgesellschaft, Germany, representing the Max-Planck Society, the Astrophysical Institute Potsdam, and Heidelberg University; The Ohio State University; and The Research Corporation, on behalf of The University of Notre Dame, University of Minnesota, and University of Virginia.

This research has made use of the SIMBAD data base, operated at CDS, Strasbourg, France. This research has made use of the NASA/IPAC Extragalactic Database (NED) which is operated by the Jet Propulsion Laboratory, California Institute of Technology, under contract with the National Aeronautics and Space Administration. This research has made use of NASA’s Astrophysics Data System.

DATA AVAILABILITY

The data underlying this article will be shared on reasonable request to the corresponding author.

REFERENCES

- Allaert F., Gentile G., Baes M., 2017, *A&A*, 605, A55
 Amorisco N. C., Evans N. W., van de Ven G., 2014, *Nature*, 507, 335
 Annibali F. et al., 2008, *AJ*, 135, 1900
 Annibali F. et al., 2013, *AJ*, 146, 144
 Annibali F. et al., 2016, *ApJ*, 826, L27
 Annibali F. et al., 2020, *MNRAS*, 491, 5101
 Athanassoula E., 2013, in Jesús F. B., Johan H. K., eds, *Secular Evolution of Galaxies. Bars and secular evolution in disk galaxies: Theoretical input*, Cambridge University Press, Cambridge, UK, p. 305
 Bacchini C., Fraternali F., Iorio G., Pezzulli G., Marasco A., Nipoti C., 2020, *A&A*, 641, A70
 Bajaja E., Huchtmeier W. K., Klein U., 1994, *A&A*, 285, 385
 Banerjee A., Patra N. N., Chengalur J. N., Begum A., 2013, *MNRAS*, 434, 1257
 Begum A., Chengalur J. N., Karachentsev I. D., 2005, *A&A*, 433, L1
 Begum A., Chengalur J. N., Kennicutt R. C., Karachentsev I. D., Lee J. C., 2008, *MNRAS*, 383, 809
 Bekki K., 2008, *MNRAS*, 388, L10
 Belokurov V., Koposov S. E., 2016, *MNRAS*, 456, 602
 Belokurov V. et al., 2006, *ApJ*, 642, L137
 Berg D. A. et al., 2012, *ApJ*, 754, 98
 Bertin E., Arnouts S., 1996, *A&AS*, 117, 393

- Bosma A., 1978, PhD thesis, University of Groningen
 Bosma A., 1981, *AJ*, 86, 1825
 Bressan A. et al., 2012, *MNRAS*, 427, 127
 Bureau M., Freeman K. C., Pfizner D. W., Meurer G. R., 1999, *AJ*, 118, 2158
 Calzetti D. et al., 2015, *ApJ*, 149, 51
 Carlin J. L. et al., 2016, *ApJ*, 828, L5
 Chen C.-W., Côté P., West A. A., Peng E. W., Ferrarese L., 2010, *ApJS*, 191, 1
 Cignoni M. et al., 2019, *ApJ*, 887, 112
 Ciotti L., Bertin G., 1999, *A&A*, 352, 447
 Combes F., 2014, *Struct. Dyn. Disk Galaxies*, 480, 211
 Cook D. O., Dale D. A., Johnson B. D. et al., 2014, *MNRAS*, 445, 881
 Côté P., Ferrarese L., Jordán A. et al., 2008, *Formation Evol. Galaxy Bulges*, 245, 395
 Crnojević D., Sand D. J., Spekkens K. et al., 2016, *ApJ*, 823, 19
 Dalcanton J. J., Williams B. F., Seth A. C. et al., 2009, *ApJS*, 183, 67
 Dale D. A., Cohen S. A., Johnson L. C. et al., 2009, *ApJ*, 703, 517
 de Vaucouleurs G., de Vaucouleurs A., Corwin H. G., Jr, Buta R. J., Paturel G., Fouque P., 1991, *Third Reference Catalogue of Bright Galaxies*, ISBN 0-387-97552-7. Springer, New York, NY, USA, p. 2091
 Deason A., Wetzel A., Garrison-Kimmel S., 2014, *ApJ*, 794, 115
 Debattista V. P., Sellwood J. A., 1998, *ApJ*, 493, L5
 Di Teodoro E. M., Fraternali F., 2015, *MNRAS*, 451, 3021
 Di Teodoro E. M., Peek J. E. G., 2021, *AJ*, 923, 23
 Diemand J., Kuhlen M., Madau P., Zemp M., Moore B., Potter D., Stadel J., 2008, *Nature*, 454, 735
 Dolphin A. E., 2000, *PASP*, 112, 1383
 Dopita M. A., Ryder S. D., 1994, *ApJ*, 430, 163
 Eigenthaler P., Puzia T. H., Taylor M. A. et al., 2018, *ApJ*, 855, 142
 Foreman-Mackey D., Hogg D. W., Lang D., Goodman J., 2013, *PASP*, 125, 306
 Fraternali F., van Moorsel G., Sancisi R., Oosterloo T., 2002, *AJ*, 123, 3124
 Gajda G., Lokas E. L., Athanassoula E., 2018, *ApJ*, 868, 100
 Gentile G., Salucci P., Klein U., Granato G. L., 2007, *MNRAS*, 375, 199
 Ghosh S., Jog C. J., 2018, *NewA*, 63, 38
 Hastings W. K., 1970, *J-BIOMETRIKA*, 57, 97
 Hayashi E., Navarro J. F., 2006, *MNRAS*, 373, 1117
 Higgs C. R., McConnachie A. W., Irwin M. et al., 2016, *MNRAS*, 458, 1678
 Ibata R., Malhan K., Martin N. et al., 2021, *ApJ*, 914, 123
 Iorio G., Fraternali F., Nipoti C., Di Teodoro E., Read J. I., Battaglia G., 2017, *MNRAS*, 466, 4159
 Johnson B. D., Weisz D. R., Dalcanton J. J. et al., 2013, *ApJ*, 772, 8
 Johnston E. J., Eigenthaler P., Puzia T. H. et al., 2019, *ApJ*, 873, 59
 Kado-Fong E., Greene J. E., Greco J. P., Beaton R., Goulding A. D., Johnson S. D., Komiyama Y., 2020, *AJ*, 159, 103
 Kallivayalil N., Sales L. V., Zivick P. et al., 2018, *ApJ*, 867, 19
 Karachentsev I. D., Kaisina E. I., 2013, *AJ*, 146, 46
 Karachentsev I. D., Dolphin A. E., Geisler D. et al., 2002, *A&A*, 383, 125
 Karachentsev I. D., Sharina M. E., Dolphin A. E. et al., 2003, *A&A*, 398, 467
 Karachentsev I. D., Karachentseva V. E., Huchtmeier W. K., Makarov D. I., 2004, *AJ*, 127, 2031
 Kennicutt R. C., Evans N. J., 2012, *ARA&A*, 50, 531
 Kennicutt R. C., Lee J. C., Funes J. G., Sakai S., Akiyama S., 2008, *ApJS*, 178, 247
 Kormendy J., Kennicutt R. C., 2004, *ARA&A*, 42, 603
 Krumm N., Burstein D., 1984, *AJ*, 89, 1319
 Lee J. C., Kennicutt R. C., Funes S. J., Shoko S., Akiyama S., 2007, *ApJ*, 671, L113
 Lelli F., Verheijen M., Fraternali F., Sancisi R., 2012a, *A&A*, 537, A72
 Lelli F., Verheijen M., Fraternali F., Sancisi R., 2012b, *A&A*, 544, A145
 Lelli F., Fraternali F., Verheijen M., 2014a, *A&A*, 563, A27
 Lelli F., Verheijen M., Fraternali F., 2014b, *A&A*, 566, A71
 Lelli F., Verheijen M., Fraternali F., 2014c, *MNRAS*, 445, 1694
 Lelli F., McGaugh S. S., Schombert J. M., 2016, *AJ*, 152, 157
 McConnachie A. W. et al., 2009, *Nature*, 461, 66
 McGaugh S. S., Lelli F., Schombert J. M., 2016, *PhRvL*, 117, 201101
 Makarova L. N., Makarov D. I., Antipova A. V., Karachentsev I. D., Tully R. B., 2018, *MNRAS*, 474, 3221
 Malhan K., Yuan Z., Ibata R., Arentsen A., Bellazzini M., Martin N. F., 2021, *ApJ*, 920, 17
 Mancera Piña P. E. et al., 2019, *ApJ*, 883, L33
 Marasco A., Oman K. A., Navarro J. F., Frenk C. S., Oosterloo T., 2018, *MNRAS*, 476, 2168
 Martínez-Delgado D. et al., 2010, *AJ*, 140, 962
 Martínez-Delgado D. et al., 2012, *ApJ*, 748, L24
 Metropolis N., Rosenbluth A. W., Rosenbluth M. N., Teller A. H., Teller E., 1953, *J. Chem. Phys.*, 21, 1087
 Meurer G. R., Carignan C., Beaulieu S. F., Freeman K. C., 1996, *AJ*, 111, 1551
 Mihos J. C., McGaugh S. S., de Blok W. J. G., 1997, *ApJ*, 477, L79
 Momany Y., Held E. V., Saviane I., Rizzi L., 2002, *A&A*, 384, 393
 Oh S.-H. et al., 2015, *AJ*, 149, 180
 Oman K. A., Marasco A., Navarro J. F., Frenk C. S., Schaye J., Benítez-Llambay A., 2019, *MNRAS*, 482, 821
 Ott J. et al., 2012, *AJ*, 144, 123
 Patra N. N., 2020, *MNRAS*, 495, 2867
 Patra N. N., Jog C. J., 2019, *MNRAS*, 488, 4942
 Paudel S., Smith R., Yoon S. J., Calderón-Castillo P., Duc P.-A., 2018, *ApJS*, 237, 36
 Peebles P. et al., 1982, *AJ*, 263, L15
 Pettitt A. R., Wadsley J. W., 2018, *MNRAS*, 474, 5645
 Posti L., Fraternali F., Di Teodoro E. M., Pezzulli G., 2018, *A&A*, 612, L6
 Privon G. C. et al., 2017, *ApJ*, 846, 74
 Pustilnik S. A., Perepelitsyna Y. A., Kniazev A. Y., 2016, *MNRAS*, 463, 670
 Randriamampandry T. H., Combes F., Carignan C., Deg N., 2015, *MNRAS*, 454, 3743
 Rich R. M. et al., 2012, *Nature*, 482, 192
 Romeo A. B., 2020, *MNRAS*, 491, 4843
 Romeo A. B., Agertz O., Renaud F., 2020, *MNRAS*, 499, 5656
 Roychowdhury S., Chengalur J. N., Begum A., Karachentsev I. D., 2010, *MNRAS*, 404, L60
 Roychowdhury S., Huang M.-L., Kauffmann G., Wang J., Chengalur J. N., 2015, *MNRAS*, 449, 3700
 Roychowdhury S., Chengalur J. N., Shi Y., 2017, *A&A*, 608, A24
 Sacchi E. et al., 2016, *ApJ*, 830, 3
 Sancisi R., Fraternali F., Oosterloo T., van der Hulst T., 2008, *A&AR*, 15, 189
 Sand D. J., Spekkens K., Crnojević D., Hargis J. R., Willman B., Strader J., Grillmair C. J., 2015, *ApJ*, 812, L13
 Schlafly E. F., Finkbeiner D. P., 2011, *ApJ*, 737, 103
 Schoenmakers R. H. M., 1999, PhD thesis, University of Groningen
 Schoenmakers R. H. M., Franx M., de Zeeuw P. T., 1997, *MNRAS*, 292, 349
 Simpson C. E., Gottesman S. T., 2000, *AJ*, 120, 2975
 Stierwalt S. et al., 2015, *ApJ*, 805, 2
 Talbot R. J., Arnett W. D., 1975, *ApJ*, 197, 551
 Thuan T. X., Goehring K. M., Hibbard J. E., Izotov Y. I., Hunt L. K., 2016, *MNRAS*, 463, 4268
 Tolstoy E., Hill V., Tosi M., 2009, *ARA&A*, 47, 371
 Tosi M. et al., 2001, *AJ*, 122, 127
 Tully R. B. et al., 2006, *AJ*, 132, 729
 Vaduvescu O., McCall M. L., Richer M. G., Fingerhut R. L., 2005, *AJ*, 130, 1593
 van Zee L., Skillman E. D., Salzer J. J., 1998, *AJ*, 116, 1186
 van Zee L., Salzer J. J., Skillman E. D., 2001, *AJ*, 122, 121
 Verheijen M. A. W., Sancisi R., 2001, *A&A*, 370, 765
 Weisz D. R. et al., 2011, *ApJ*, 739, 5
 Wheeler C. et al., 2015, *MNRAS*, 453, 1305
 White S. D. M., Rees M. J., 1978, *MNRAS*, 183, 341
 Zhang H.-X., Smith R., Oh S.-H. et al., 2020, *ApJ*, 900, 20

APPENDIX A: PROJECTED MASS PROFILE OF THE OLD STELLAR COMPONENT

We fitted the old stellar component (projected) mass profile using individual star counts. To do this, we started from the *HST* ACS

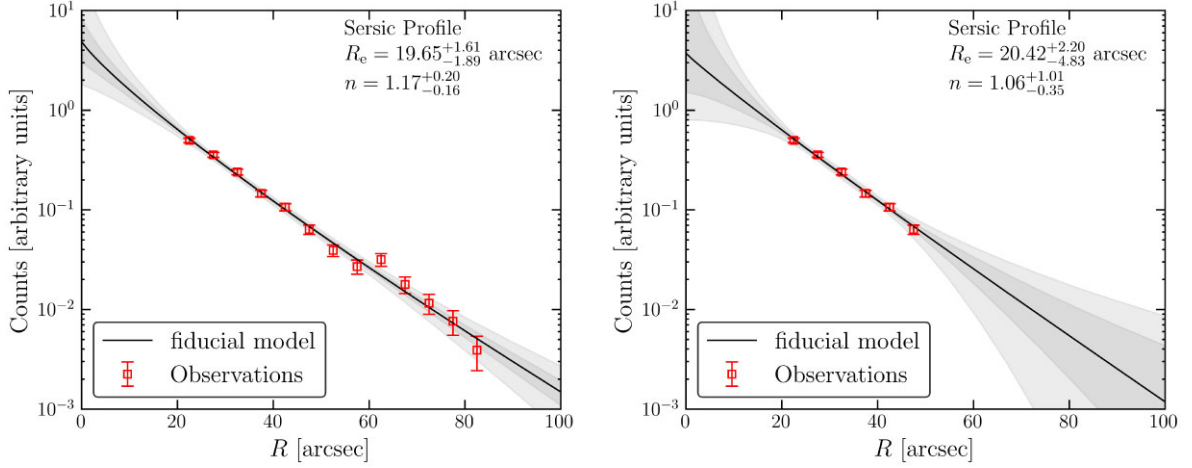


Figure A1. Fit to the old component stellar profile. Red squares denote the observed RGB counts, while the solid line is our best fit. The grey shaded area delimits the 16th and 84th percentile region of uncertainty. The fit in the left-hand panel was obtained considering all star counts within a galacto-centric distance of $20 < R < 85$ arcsec, while the fit to the right-hand panel was restricted to a smaller $20 < R < 50$ arcsec range.

photometric catalogue described in Section 2.2 and selected RGB stars down to 2 mag fainter than the RGB tip. We assume that star counts on the RGB trace the old stellar mass. We considered only stars with galacto-centric distances between 20 and 85 arcsec: star counts within 20 arcsec from the galaxy centre are highly affected by incompleteness due to severe crowding, while star counts beyond 85 arcsec can be significantly affected by background galaxies’ contamination. The counts were binned into $N = 13$ concentric circular annuli centred on the galaxy nominal centre. Thus, the profile consists of a set of $\mathcal{D} \equiv \{R_i, n_i, \delta n_i\}$ points, with $i = 1, \dots, N$, where R_i is the average distance of the i -th bin, n_i the stellar counts in that bin and δn_i the associated Poisson error. To derive the system effective radius (i.e. the distance on the plane of the sky that contains half of the stellar mass), we fit the profile with a Sérsic model

$$n(R) = n_0 \exp \left[b_m \left(\frac{R}{R_e} \right)^{\frac{1}{m}} \right], \quad (\text{A1})$$

where n_0 is the normalization, R_e the effective radius, m the Sérsic index, and b_m as in equation (18) of Ciotti & Bertin (1999). To explore the parameter space, we used a Markov chain Monte Carlo (MCMC) method. The log-likelihood of the model $\ln \mathcal{L}(\xi|\mathcal{D})$, defined by the parameter vector $\xi = \{n_0, R_e, m\}$, given the data \mathcal{D} is

$$\ln \mathcal{L}(\xi|\mathcal{D}) = -\frac{1}{2} \sum_{i=1}^N \left(\frac{n(R_i) - n_i}{\delta n_i} \right)^2. \quad (\text{A2})$$

We ran 16 chains, each evolved for 4000 steps, we used a Metropolis–Hastings sampler (Metropolis et al. 1953; Hastings 1970) to sample from the posterior, and we used flat priors over the models’ free parameters. The MCMC was run by means of the `emcee` library (Foreman-Mackey et al. 2013). We eliminated the first 2000 steps of each chain as conservative burn-in and we used the remaining steps to build the posterior distributions over the model’s free parameters. According to our fit, the estimated effective radius is $R_e = 19.65^{+1.61}_{-1.89}$ arcsec, while the Sérsic index is $m = 1.17^{+0.20}_{-0.16}$, where the quoted errors have been computed as the 16th and 84th percentiles of the corresponding marginalized one dimensional

distributions. The result of the fit is shown in the left-hand panel of Fig. A1. Since the more external bins may be contaminated by stars of the Tail, we tested our estimate of R_e also fitting the projected number density profile with bins in a smaller radial range of $20 < R < 50$ arcsec (right-hand panel). Although with larger errors, the inference over the models free parameters is consistent with the previous case, especially for the estimate of the effective radius ($R_e = 20.42^{+2.20}_{-4.83}$, $m = 1.06^{+1.01}_{-0.35}$). In the end, we estimate the total magnitude of the old stellar component from the fitted profile parameters. To this purpose, we first perform aperture photometry on the LBT images deriving a surface brightness of $\mu_g = 26.3 \pm 0.3$ mag arcsec $^{-2}$ and $\mu_r = 26.5 \pm 0.3$ mag arcsec $^{-2}$ in an external galaxy region at $40 < R < 45$ arcsec not contaminated by young stars; then, once the Sérsic profile is normalized to these values, we derive total magnitudes of $M_g = -12.5 \pm 0.3$ and $M_r = -12.3 \pm 0.3$ for the old stellar component.

APPENDIX B: RADIAL PROFILES OF THE H I DISTRIBUTION AND KINEMATICS

This section provides the H I rotation curve, the radial profile of the H I velocity dispersion, and the azimuthally averaged radial profile of the H I surface density for the three best-fitting models presented in Section 3. These profiles are shown in Fig. B1, where we also provide a comparison with the H I rotation curve from Allaert et al. (2017), the H I velocity dispersion from Gentile et al. (2007), and the H I surface density from Begum et al. (2008). The rotation curves and the velocity dispersion radial profiles of our models are perfectly in agreement, within the uncertainties, with each other and with the literature (i.e. Gentile et al. 2007; Allaert et al. 2017). We note that, beyond $R \simeq 4$ kpc, the velocity dispersion profile derived by Gentile et al. (2007) from the second moment map of the WSRT data cube is slightly lower than our profiles, but the associated uncertainties are not available. The H I surface density obtained by Begum et al. (2008) from the GMRT data cube is only grossly similar to our profile, but this could be due to the different data and masking method.

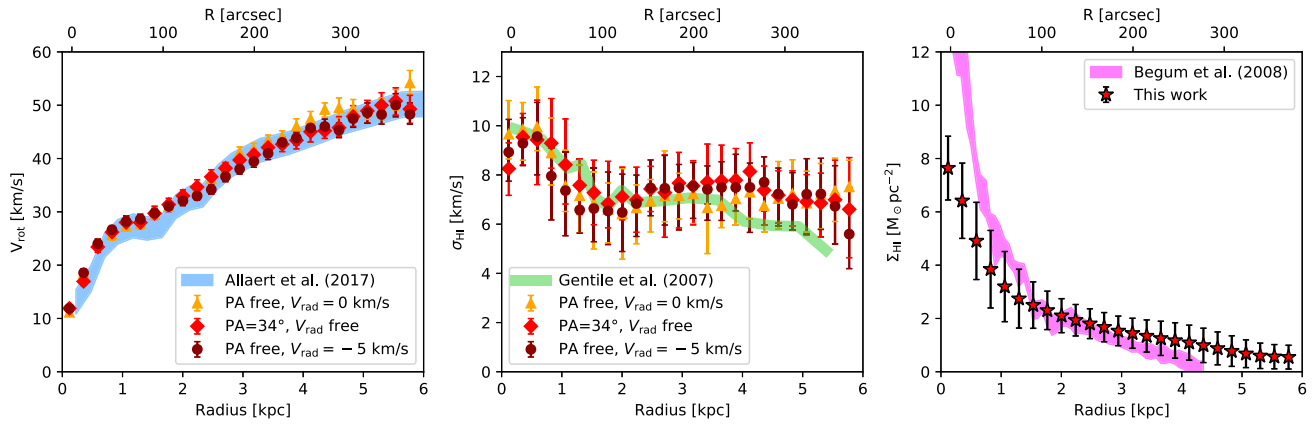


Figure B1. H I rotation curve (left-hand panel), radial profile of the H I velocity dispersion (centre), and azimuthally averaged radial profile of the H I surface density (right-hand panel) for the three best-fitting models obtained using 3^{D} BAROLO. The blue, green, and magenta curves in the three panels are the H I rotation curve from Allaert et al. (2017), the H I velocity dispersion profile from Gentile et al. (2007), and the H I surface density from Begum et al. (2008), respectively.

This paper has been typeset from a $\text{\TeX}/\text{\LaTeX}$ file prepared by the author.